nature photonics

ARTICLES

PUBLISHED ONLINE: 24 NOVEMBER 2014 | DOI: 10.1038/NPHOTON.2014.269

Small-molecule solar cells with efficiency over 9%

Qian Zhang[1†], Bin Kan[1†], Feng Liu[2†], Guankui Long[1], Xiangjian Wan[1], Xiaoqing Chen[3], Yi Zuo[1], Wang Ni[1], Huijing Zhang[1], Miaomiao Li[1], Zhicheng Hu[4], Fei Huang[4], Yong Cao[4], Ziqi Liang[3], Mingtao Zhang[5], Thomas P. Russell[2] and Yongsheng Chen[1*]

At present, state-of-the-art single-junction organic photovoltaic devices have power conversion efficiencies of >9% and >8% for polymer- and small-molecule-based devices, respectively. Here, we report a solution-processed organic photovoltaic device based on DRCN7T, which employs an oligothiophene-like small molecule with seven conjugation units as the backbone and 2-(1,1-dicyanomethylene)rhodanine as the terminal unit. With [6,6]-phenyl C_{71}-butyric acid methyl ester ($PC_{71}BM$) as the acceptor, an optimized power conversion efficiency of 9.30% (certified at 8.995%) is achieved. The DRCN7T-based devices have a nearly 100% internal quantum efficiency, which we believe is due to an optimized nanoscale interpenetrating donor/acceptor network (with highly crystalline donor fibrils with diameters of ~10 nm, close to the exciton diffusion length in organic materials) and the use of an efficient electron transport layer.

Organic photovoltaic devices (OPVs), with their advantages of low cost and flexibility, are a promising platform with which to address, in part, the increasing global energy demands. Polymer-based OPVs (P-OPVs) have achieved power conversion efficiencies (PCEs) of >9% for single-junction devices[1,2] and 10.6% for tandem devices[3]. Small-molecule-based OPVs (SM-OPVs)[4–6], on the other hand, have reported efficiencies of >8% for single-junction devices[7–9] and over 12% for tandem devices[10], and have the distinct advantages of having well-defined structures (as a consequence of less batch-to-batch variation[11,12]) and generally higher open-circuit voltages (V_{OC})[13]. Even with these significant advances, the relatively low PCEs are detrimental for commercial application[14]. Due to the complicated and multi-step photoelectron conversion processes—including light harvesting, exciton diffusion and dissociation, charge transport and collection steps[15]—it is necessary to strike a delicate balance between molecular design[4–6,16–20], morphology[21,22], interfacial layer[23–25] and device fabrication[26,27] to maximize the PCEs[28]. As $PCE = V_{OC} \times J_{SC} \times FF/P_{in}$, where J_{SC} is the short-circuit current density, FF is the fill factor and P_{in} is the incident light intensity, the main challenge for SM-OPVs is to enhance the FF and J_{SC} while maintaining the V_{OC} through better molecular design, morphology control and interfacial engineering.

Recently, we have reported that a series of oligothiophene-like small molecules with seven conjugation units in the backbone exhibited excellent performance[5] and, using an ethylrhodanine end group, J_{SC} was improved significantly[29]. In this Article, a new molecule (Fig. 1a), 2,2′-((5Z,5′Z)-5,5′-((3,3′′′′,3′′′′′,3′′′′′′,4′,4′′-hexaoctyl-[2,2′:5′,2′′:5′′,2′′′:5′′′,2′′′′:5′′′′,2′′′′′:5′′′′′,2′′′′′′-sepithiophene]-5,5′′′′′′-diyl)bis(methanylylidene))bis(3-ethyl-4-oxothiazolidine-5,2-diylidene))dimalononitrile (abbreviated DRCN7T), using 2-(1,1-dicyanomethylene)rhodanine as the terminal unit, was designed and its OPV performance was systematically investigated. A PCE of 9.30% (certified at 8.995%), with $J_{SC} = 14.87$ mA cm^{-2} and FF = 68.7%, was achieved. This is the highest PCE for single-junction SM-OPVs reported to date[7–9,26]. This remarkable performance arises from a network of highly crystalline donor fibrils with ~10 nm diameters, which is close to the exciton diffusion length[30] (Fig. 1b), and the use of an efficient electron transport layer (ETL). Both theoretical and experimental results indicate that optimal efficiency is achieved for exciton diffusion/dissociation and charge transport/collection with little geminate or non-geminate recombination. These combine to produce an internal quantum efficiency (IQE) close to 100%, which is mandatory to evaluate the intrinsic OPV performance of any material and achieve high performance.

Molecular design and characterization

DRCN7T was designed with only a very small structural change to (5Z,5′Z)-5,5′-((3,3′′′′,3′′′′′,3′′′′′′,4′,4′′-hexaoctyl-[2,2′:5′,2′′:5′′,2′′′:5′′′,2′′′′:5′′′′,2′′′′′:5′′′′′,2′′′′′′-sepithiophene]-5,5′′′′′′diyl) bis(methanylylidene))bis(3-ethyl-2-thioxothiazolidin-4-one) (DERHD7T)[29] by replacing the thio group with a dicyanomethylene group (Fig. 1a), as the dicyanomethylene group has been used as a strong and efficient electron-accepting group to enhance light absorption[31]. Density functional theory (DFT) calculations indicate that this small change could lower the bandgap (mainly due to its lower lowest unoccupied molecular orbital, LUMO) (Supplementary Table 2) and enhance absorption (Supplementary Fig. 1a). The introduction of the dicyanomethylene group could also increase the ground state dipole moment and enhance the electronic coupling between neighbouring molecules (Supplementary Tables 3 and 4), which would promote crystallization. Also, with this change, the molecular hole reorganization energy is expected to decrease[32] (Supplementary Table 3). All these factors would suggest that a balanced charge transport and therefore an enhanced FF would be expected in OPVs based on DRCN7T[33].

In $CHCl_3$ solution, DRCN7T shows a bathochromic absorption peak at 530 nm (compared with the 508 nm peak for DERHD7T) and also has a higher maximal absorption coefficient of 47 l g^{-1} cm^{-1}, both of which are consistent with the calculated results

[1]Key Laboratory for Functional Polymer Materials and Center for Nanoscale Science and Technology, Institute of Polymer Chemistry and Synergetic Innovation Center of Chemical Science and Engineering (Tianjin), College of Chemistry, Nankai University, Tianjin, 300071, China. [2]Polymer Science and Engineering Department, University of Massachusetts, Amherst, Massachusetts 01003, USA. [3]Department of Material Science, Fudan University, Shanghai, 200433, China. [4]Institute of Polymer Optoelectronic Materials and Devices, State Key Laboratory of Luminescent Materials and Devices, South China University of Technology, Guangzhou, 510640, China. [5]Computational Center for Molecular Science, College of Chemistry, Nankai University, Tianjin, 300071, China. †These authors contributed equally to this work. *e-mail: yschen99@nankai.edu.cn

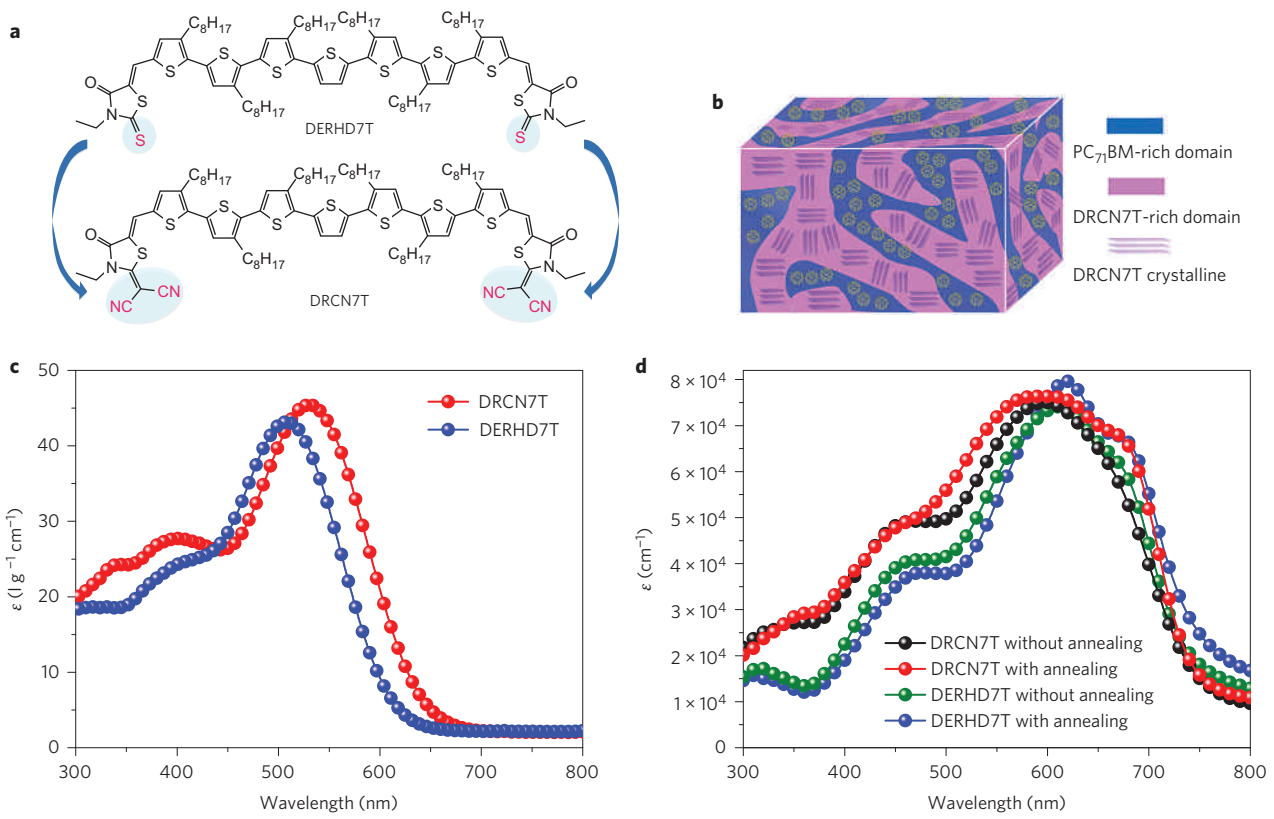

Figure 1 | Molecular design and characterization. a, Chemical structures of DRCN7T and DERHD7T. **b**, Schematic morphology of the active layer based on DRCN7T:$PC_{71}BM$ under optimized conditions. **c**, UV–vis absorption spectra of DRCN7T and DERHD7T in chloroform solution. **d**, UV–vis absorption spectra of neat DRCN7T and DERHD7T films with and without thermal annealing at 90 °C for 10 min. ε in **c**,**d** refers to the absorption coefficient.

(Supplementary Fig. 1a). Although both molecules show a significant redshift in absorption in the solid state, DRCN7T exhibits a wider and overall stronger absorption up to 760 nm (Supplementary Table 1). After thermal annealing, DRCN7T shows a broader and generally stronger absorption than DERHD7T. Also, the vibronic shoulder peak at 676 nm indicates enhanced crystallinity and effective π–π stacking between the molecular backbones. Better absorption was also observed for DRCN7T mixed with the acceptor than DERHD7T (Supplementary Fig. 1b). More importantly, results for the active layers in real devices with a reflection geometry-spectrometer[34] (Supplementary Fig. S3) and optical simulations based on an optical transfer matrix model[35,36] (Supplementary Fig. 5) show a similar trend. As expected, the optical bandgap of DRCN7T (1.62 eV) is lower than that of DERHD7T (1.69 eV). This is also consistent with cyclic voltammetry (CV) studies and DFT calculations (Supplementary Table 2).

Photovoltaic performance

DRCN7T shows high solubility in common solvents, excellent thermal stability (Supplementary Fig. 7) and good film-forming properties for solution processing. OPVs using fullerene derivatives as the electron acceptor were fabricated, with varying donor/acceptor ratios, film thicknesses, annealing temperatures and ETLs (as shown in Supplementary Section 8). The best performance was obtained with the device structure indium tin oxide (ITO)/PEDOT:PSS/DRCN7T:$PC_{71}BM$/PFN/Al when the weight ratio of donor and acceptor was 1:0.5 and with thermal annealing at 90 °C for 10 min. Under these conditions, a PCE of 9.30% (certified at 8.995%) with $V_{OC} = 0.91$ V, $J_{SC} = 14.87$ mA cm^{-2} and FF = 68.7% was achieved. Note that the devices with poly[(9,9-bis(3′-(*N*,*N*-dimethylamino)propyl)-2,7-fluorene)-*alt*-2,7-(9,9-dioctylfluorene)] (PFN), a widely investigated ETL material[37], give higher and more reproducible performance than other ETL-based devices using LiF and ZnO, for example (Supplementary Figs 15, 16 and Table 10)[38]. This enhanced performance with PFN as the ETL could be due to the reduced energy barrier between the active layer and metal electrode, thus improving charge transport and collection efficiency (see also Supplementary Section 9)[25]. For comparison, DERHD7T:$PC_{71}BM$-based devices were fabricated under the same conditions, and the corresponding optimized results for both materials are shown in Table 1. Note that DRCN7T performs significantly better than DERHD7T.

The characteristic current density–voltage (J–V) curves of the optimized devices based on these two materials under the same conditions are presented in Fig. 2a with PFN as the ETL. As seen in Table 1, although the devices based on these two compounds give a similar high V_{OC} of ~0.9 V, as expected from their comparable

Table 1 | Photovoltaic performance of DRCN7T- and DERHD7T-based devices under the same optimized conditions (device structure, ITO/PEDOT:PSS/active layer/ETL/Al).

Donor	V_{OC} (V)	J_{SC} (mA cm^{-2})	FF (%)	PCE (%)	
				Best	Average
DRCN7T*	0.91	14.87	68.7	9.30	9.05
DERHD7T*	0.89	9.49	51.6	4.35	4.25
DRCN7T†	0.90	14.51	58.2	7.60	7.55
DERHD7T†,‡	0.92	13.98	47.4	6.10	5.88

*The ETL is PFN, using the same conditions for optimized DRCN7T-based devices. †The ETL is LiF under the corresponding optimized conditions for both individual molecules. ‡Data from ref. 29, using $PC_{61}BM$ as the acceptor.

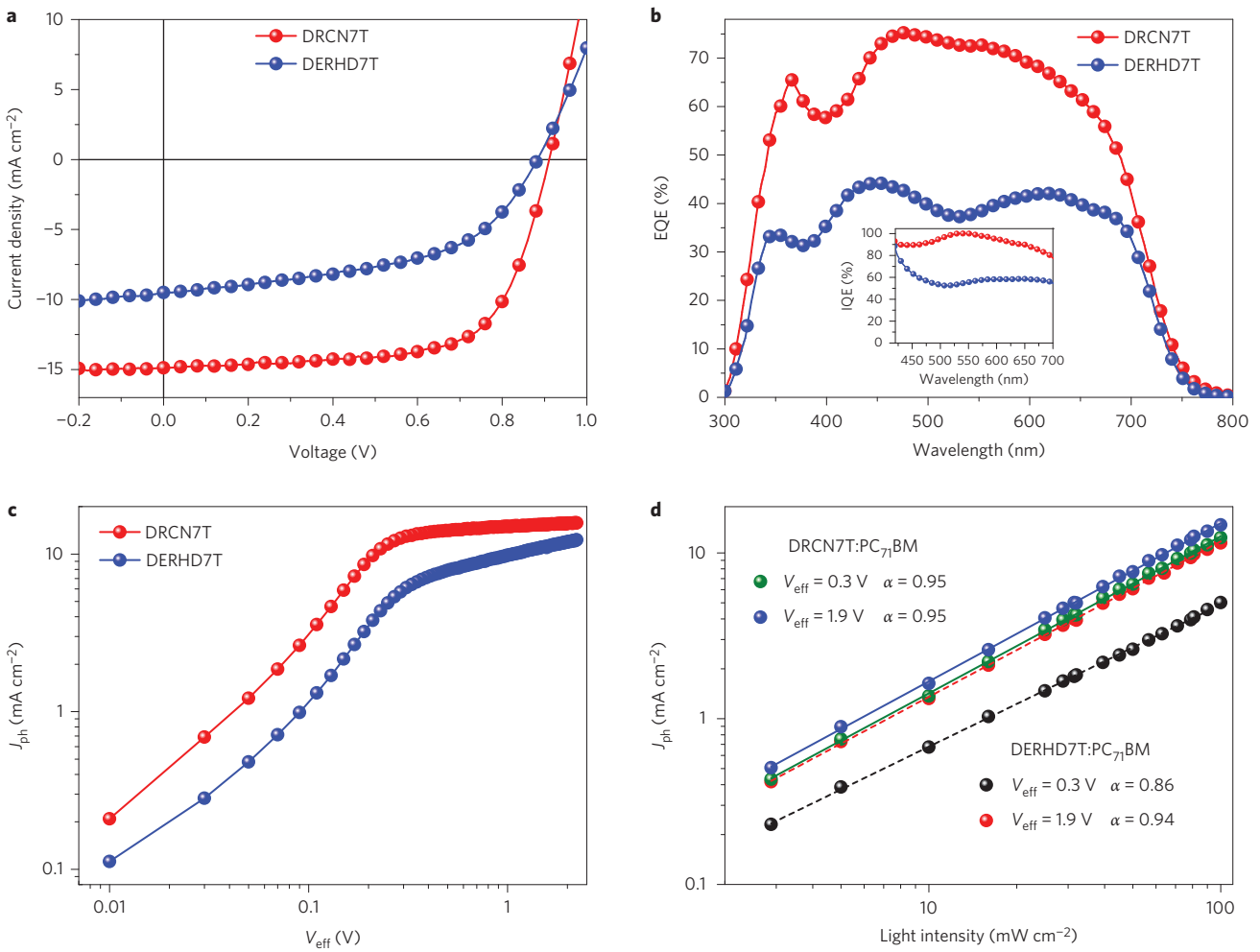

Figure 2 | Device performance with structure ITO/PEDOT:PSS/DRCN7T:$PC_{71}BM$ or DERHD7T:$PC_{71}BM$/PFN/Al. a, Characteristic current density versus voltage (J–V) curves of both devices under optimized conditions and simulated AM 1.5G irradiation (100 mW cm^{-2}). **b**, EQE curves for both devices. Inset: corresponding IQE spectra. **c**, Photocurrent density versus effective voltage (J_{ph}–V_{eff}) characteristics for both devices under constant incident light intensity (AM 1.5G, 100 mW cm^{-2}). **d**, Double logarithmic plots of photocurrent density as a function of incident light intensity for both devices under effective voltages of 1.9 and 0.3 V. Lines represent the best power fitting.

highest occupied molecular orbitals (HOMOs), their J_{SC} and FF values differ markedly.

The external quantum efficiency (EQE) curve of the best device based on DRCN7T is presented in Fig. 2b, which gives a much higher EQE (mostly at 60–75%) than that of DERHD7T-based devices over the entire solar spectral range. The calculated J_{SC} value (14.37 mA cm^{-2}) obtained from the integration of EQE data for the DRCN7T-based device is close to the J_{SC} value (14.87 mA cm^{-2}) from the J–V measurement, with a 3.3% mismatch. The effective PCE of the active layer should be judged by the IQE, which is calculated from the measured effective absorption of the active layer and the EQE, as shown in the inset of Fig. 2b. This shows that the IQE for the DRCN7T-based device exceeds 90% from 450 to 650 nm and at ~520 nm it is close to 100%. Consequently, almost every photon absorbed by the active layer is converted into free charges *and* collected[34], demonstrating that, in the multi-step photoelectron conversion process, each of the steps is highly efficient with little geminate or non-geminate recombination. This is in marked contrast with the DERHD7T-based device, where the IQE was <60% over most of the solar spectral range.

The high performance of DRCN7T-based devices and the significant difference compared with DERHD7T-based devices are supported by the relation of photocurrent density (J_{ph}) versus effective voltage (V_{eff}) or light intensity (P_{in}). $J_{ph} = J_L - J_D$, where J_L and J_D are the current densities under illumination and in the dark, respectively. For $V_{eff} = V_o - V_a$, V_o is the voltage at which $J_{ph} = 0$ and V_a is the applied voltage. A plot of J_{ph} versus V_{eff}[15] is presented in Fig. 2c. For DRCN7T-based devices, J_{ph} has a nearly linear dependence on the voltage at a low value of V_{eff}, and J_{ph} reaches saturation (where saturation current density J_{sat} was obtained) when the effective voltage V_{eff} arrives at a relatively low voltage of 2 V. This suggests that the photogenerated excitons are dissociated into free charge carriers *and* charge carriers are collected at the electrodes very efficiently, with little geminate or bimolecular recombination for DRCN7T-based devices. However, for the DERHD7T case, the J_{ph} shows a stronger field-dependence across a large bias range and has not fully saturated even at $V_{eff} = 3$ V (Supplementary Fig. 17), suggesting a significant geminate and/or bimolecular recombination and/or less efficient interfacial contact, thus a lower FF[39–41]. The ratio J_{ph}/J_{sat} can be used to judge the overall exciton dissociation efficiency and charge collection efficiency[37]. Under short-circuit conditions, the ratios are 95% and 81% for DRCN7T- and DERHD7T-based devices, respectively, indicating a much higher exciton dissociation efficiency for DRCN7T-based devices. At the maximal power output conditions, J_{ph}/J_{sat} is 80% and 61% for the DRCN7T- and DERHD7T-based devices, respectively, also indicating a higher charge collection

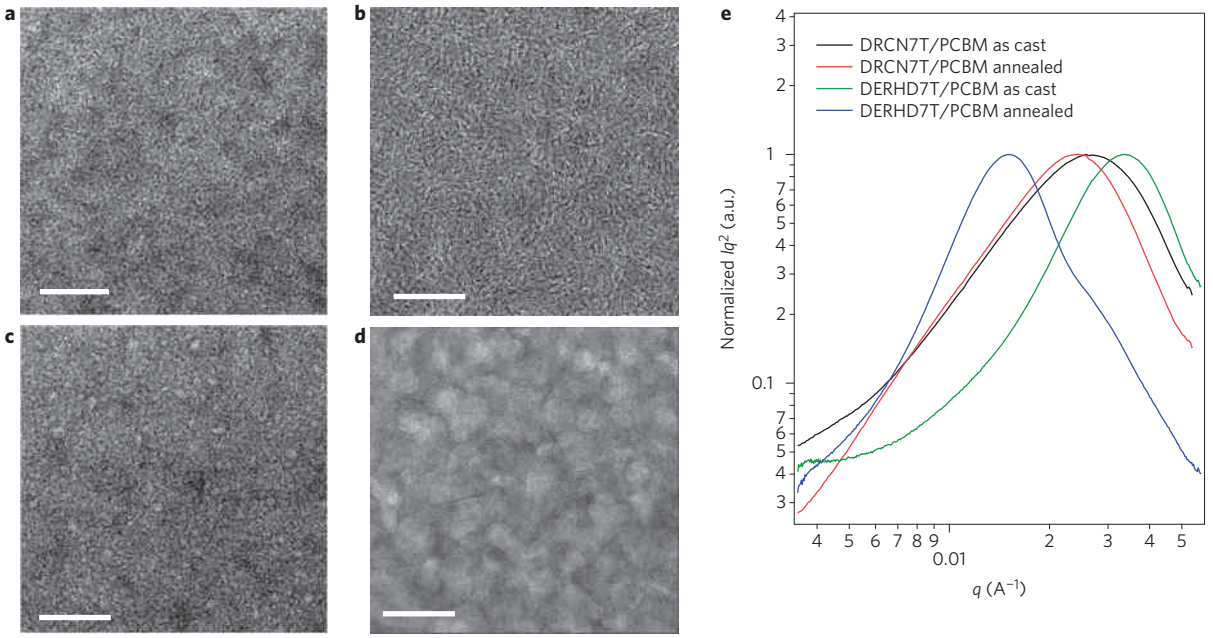

Figure 3 | Morphology of blend films. a,**b**, TEM images of the DRCN7T:PC$_{71}$BM (1:0.5, wt/wt) blend films without (**a**) and with (**b**) thermal annealing. **c**,**d**, TEM images of the DERHD7T:PC$_{71}$BM (1:0.5, wt/wt) blend films without (**c**) and with (**d**) thermal annealing. Scale bars, 200 nm. **e**, RSoXS profiles of DRCN7T:PC$_{71}$BM and DERHD7T:PC$_{71}$BM films with and without annealing. Iq^2, intensity × q^2. a.u., arbitrary units.

efficiency and less bimolecular recombination for DRCN7T-based devices[37]. In addition, the DRCN7T-based device has a larger shunt resistance (1,260 versus 320 Ω cm^2) and smaller series resistance (6.0 versus 16.5 Ω cm^2) than for the DERHD7T-based device, indicating that better ohmic contact is formed in the DRCN7T-based device.

When the build-up of space charges reaches a fundamental limit, the photocurrent J_{ph} will scale with P_{in} as $J_{ph} \propto P_{in}^{\alpha}$ with $\alpha = ¾$, and if there is no space charge build-up, $\alpha = 1$ (ref. 42). As shown in Fig. 2d, at a high effective voltage ($V_{eff} = 1.9$ V) $\alpha \approx 1$ (0.95 and 0.93 for DRCN7T- and DERHD7T-based devices, respectively). At low effective voltages ($V_{eff} = 0.3$ V) corresponding to an external bias of 0.73 V, where the maximal power output is observed, $\alpha = 0.95$ for the DRCN7T-based device, but it decreases to 0.86 for the DERHD7T-based device. These results suggest a little build-up of space charge and bimolecular recombination for the DRCN7T-based device, but not for the DERHD7T case, consistent with the better interfacial contact for the DRCN7T case discussed above. This is also supported by the hole and electron mobility results for the blend of these two materials with PC$_{71}$BM measured using the space-charge limited current (SCLC) method (Supplementary Tables 16 and 17). The hole and electron mobilities for the DRCN7T:PC$_{71}$BM blend are ~5.91×10^{-4} and ~1.28×10^{-4} cm^2 V^{-1} s^{-1}, respectively. However, the hole and electron mobilities for the DERHD7T:PC$_{71}$BM blend (1.18×10^{-4} and 1.04×10^{-5} cm^2 V^{-1} s^{-1}) are much less balanced. Note that the SCLC hole mobilities of both neat DRCN7T and its blend films are higher than for the DERHD7T cases, which is consistent with results obtained using the photo-induced carrier extraction by linearly increasing the voltage (photo-CELIV) method (Supplementary Fig. 21)[43]. Furthermore, in the plot of J_{SC} as a function of light intensity P_{in}, $J_{ph} \propto P_{in}^{\alpha}$, the power-law exponents α are 0.96 and 0.93 for DRCN7T and DERHD7T devices, respectively (Supplementary Fig. 22), indicating less bimolecular recombination in the DRCN7T-based devices[8].

Film morphology analysis

The morphology of the active layer can be a determining factor for OPV performance. From atomic force microscopy (AFM) measurements, films of DRCN7T and DERHD7T blended with PC$_{71}$BM yielded root-mean-square (r.m.s.) surface roughnesses of only 0.39 and 0.57 nm, respectively (Supplementary Fig. 24). After annealing, the roughness for the DRCN7T blend film did not change, whereas the roughness for the DERHD7T blend film increased markedly to 2.7 nm. Transmission electron microscopy (TEM) studies (Fig. 3) show that the morphologies of the blend films for these two compounds are quite different. DRCN7T:PC$_{71}$BM mixtures (Fig. 3a) show a network of fibrils with diameters of ~10 nm (comparable to the exciton diffusion length[30]), which should favour high exciton diffusion/dissociation efficiency[44]. However, a less defined phase separation was found for the DERHD7T:PC$_{71}$BM blend (Fig. 3c). With annealing, the difference became even more pronounced, with the fibrillar network morphology being retained and strengthened for the DRCN7T:PC$_{71}$BM mixture (Fig. 3b), while the phase-separated morphology of the DERHD7T:PC$_{71}$BM mixture coarsened significantly (Fig. 3d), with a domain size of ~30–70 nm. Thus, in the DERHD7T case, excitons will have a higher probability of recombining before reaching the donor–acceptor interface, resulting in low exciton diffusion/dissociation

Table 2 | Morphology data of out-of-plane GIXD and RSoXS.

Materials	(100) *d* spacing (Å)	(100) crystal size (Å)	(010) *d* spacing (Å)	(010) crystal size (Å)	Ratio of face-on/ edge-on area	Centre-to-centre distance (nm)
DRCN7T:PC71BM as cast	20.8	126	3.54	37.5	2.4	22
DRCN7T:PC71BM annealed	20.5	148	3.56	37.8	1.7	26
DERHD7T:PC71BM as cast	21.8	107	3.65	48.0	1.6	19
DERHD7T:PC71BM annealed	21.2	150	3.65	66.2	1.2	42

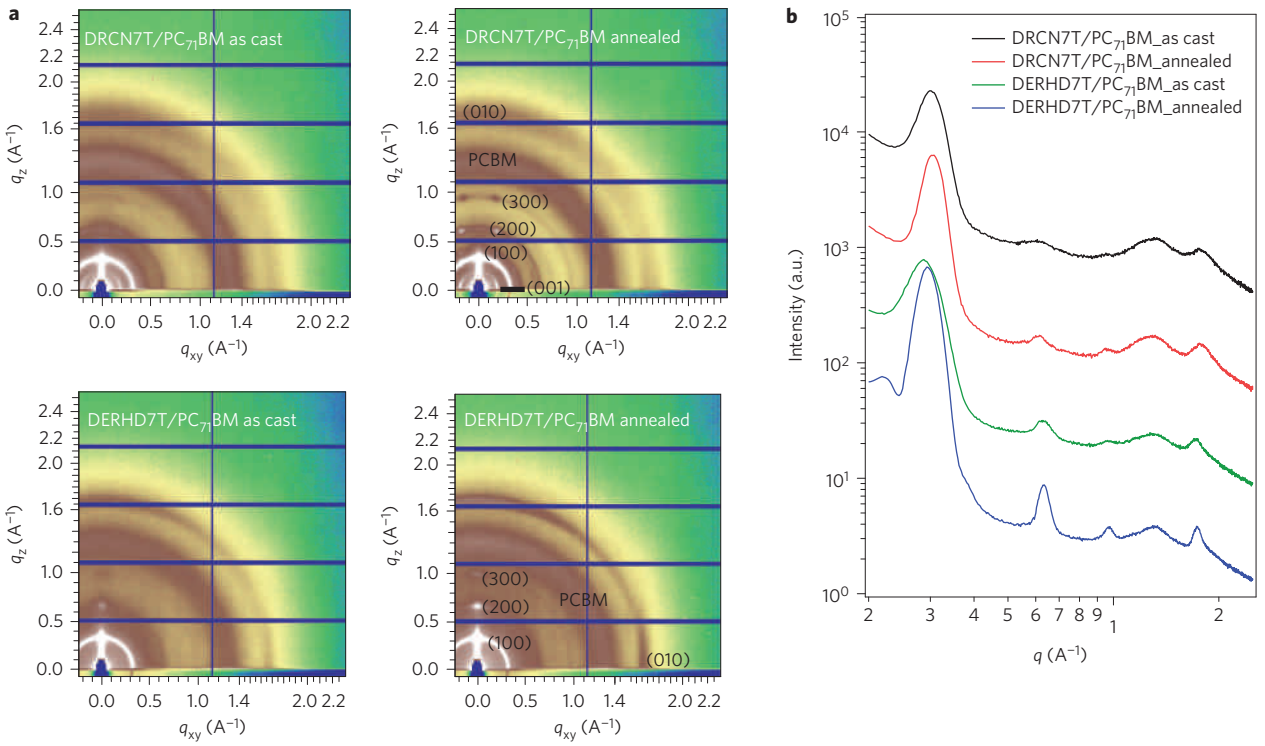

Figure 4 | GIXD data of the blend films. a, GIXD profiles of DRCN7T:PC_{71}BM and DERHD7T:PC_{71}BM blend films with and without annealing. **b**, Out-of-plane line-cuts of GIXD of blend films. a.u., arbitrary units.

efficiency. As would be expected from these morphological differences, a higher photoluminescence quenching efficiency (91%) is observed for the DRCN7T active layer in comparison to that of the DERHD7T active layer (82%, Supplementary Fig. 23).

Resonant soft X-ray scattering (RSoXS) (Fig. 3e) on the DERHD7T:PC_{71}BM blend showed an interference ($q = 0.0033$ Å^{-1}, where q is the scattering vector) corresponding to a domain centre-to-centre distance of 19 nm, which increased to 42 nm with thermal annealing (Table 2). This is consistent with the coarsening of the morphology observed by TEM. The DRCN7T:PC_{71}BM blends, on the other hand, retain a much finer texture, with an interference at $q \approx 0.0029$ Å^{-1}, corresponding to a centre-to-centre distance of 22 nm, which did not change significantly upon annealing. Note that one-half of this centre-to-centre distance is close to the ideal exciton diffusion distance. These results are consistent with the morphological results measured by AFM and TEM, indicating a more favourable exciton diffusion/dissociation in DRCN7T devices.

As the local molecular ordering and orientation also have a great impact on the exciton diffusion/dissociation and charge transport/collection, even with an ideal domain size, grazing incidence X-ray diffraction (GIXD) was used to further characterize the microstructural features of the neat DERHD7T and DRCN7T films (Supplementary Fig. 25) and their blends with PC_{71}BM (Fig. 4). Out-of-plane line-cuts are also shown, together with the 2D diffraction profiles. In all cases, multiple higher-order (h00) reflections, characteristic of the separation distance between adjacent oligothiophene backbones, are evident, indicating a long-range order and crystallinity in the films. Thermal annealing significantly improves the crystalline order, which is demonstrated in the quantitative data for the crystal size, estimated by the Scherrer equation (Table 2 and Supplementary Table 18). This would also enhance the charge transport and improve mobilities (Supplementary Tables 16 and 17). For example, the hole mobility for the DRCN7T:PC_{71}BM blend without thermal annealing is 6.99×10^{-5} cm^2 V^{-1} s^{-1}, which increased to 5.91×10^{-4} cm^2 V^{-1} s^{-1} after thermal annealing. For the neat DRCN7T film with thermal annealing, an intense reflection with higher orders is seen at a Bragg distance of ~3 nm (0.2 Å^{-1}) oriented at 17° with respect to the surface plane (Supplementary Fig. 26). This corresponds to the interlayer distance (the 001 spacing). However, this is not observed in the DERHD7T neat film. For the blend films with thermal annealing, DRCN7T showed a large azimuthal distribution of the (100) peak, while DERHD7T showed the preferred edge-on orientation normal to the surface of the films (Fig. 4a). In addition, from the ratio of the areas under the out-of-plane and in-plane π-stacking reflections (Table 2), DRCN7T showed a more prominent face-on orientation, with a ratio of 1.7, which is larger than that of DERHD7T (ratio of 1.2). Furthermore, a 3.56 Å π–π stacking distance is seen in the DRCN7T:PC_{71}BM blend film, which is slightly smaller than that of DERHD7T (3.65 Å) (Table 2). All these factors favour charge transport in the DRCN7T devices[45].

It should be noted that in the DRCN7T:PC_{71}BM blend film with thermal annealing, fibrillar crystalline domains are enhanced by the PC_{71}BM segregating into the intercrystalline domains[22]. The crystal size (~15 nm, Table 2) along the (100) direction of DRCN7T is quite close to the entire domain size, as measured by TEM, which suggests that one of the phases of the active layer observed in TEM is a highly ordered DRCN7T phase[46]. This highly crystalline fibrillar-type morphology enhances the p-type domain connectivity, which eventually improves hole transport across the film, correlated to a high FF for the OPV device. In the DERHD7T:PC_{71}BM blends, thermal annealing significantly increased the size of phase separated domains up to ~30–70 nm, which is much larger than the corresponding crystal size (~15 nm), leading to a low J_{SC} in devices. These large domains also break the connectivity of PC_{71}BM domains, as reflected in the lower electron mobility compared to that of DRCN7T in the film above (Supplementary Table 17), which could lead to a lower FF in such devices. The combination of the small size scale of the fibrils (~10 nm) and the phase-separated morphology, highly crystallized domains, tight π–π overlap and

favourable crystal orientation lead to an exceptional device performance of DRCN7T blends.

Conclusions

We have shown that a rather small change in the molecular design can lead to marked differences in the structure and performance of materials. In devices based on DRCN7T, a morphology with an optimized interpenetrating network consisting of ~10-nm-diameter highly crystalline fibrils is obtained, so little geminate or non-geminate recombination is observed. All these factors, combined with the efficient ETL (PFN), result in an ~100% IQE. Together with the improved light absorption, DRCN7T-based devices exhibit PCEs as high as 9.30%. Further studies are needed to understand the reasons why such a small end-group change can make such a large difference to the morphology and device performance. We note that 10% of the light was reflected even with an optimized device. Consequently, with an improved device structure, PCEs could be enhanced significantly.

Methods

The DRCN7T was synthesized as described in the Supplementary Information, and $PC_{71}BM$ was purchased from American Dye Source. PFN was obtained from SCUT with a number molecular weight (M_n) of 9,272 and a polydispersity of 1.473. All materials were used as received unless specified. Detailed synthesis and characterizations for DRCN7T including NMR, CV and other additional data are provided in the Supplementary Information.

Solar cell fabrication and testing. Devices were fabricated with a structure of glass/ITO/PEDOT:PSS/donor:acceptor/ETL/Al. The ITO-coated glass substrates were cleaned by ultrasonic treatment in detergent, deionized water, acetone and isopropyl alcohol under ultrasonication for 15 min each, and subsequently dried by a nitrogen blow. A thin layer of PEDOT:PSS (Clevios P VP AI 4083, filtered at 0.45 μm) was spin-coated at 3,000 r.p.m onto the ITO surface. After being baked at 150 °C for 20 min, the substrates were transferred into an argon-filled glove box. Subsequently, the active layer was spin-coated from blend chloroform solutions with different ratios (weight-to-weight) of DRCN7T and $PC_{71}BM$ and then annealed at different temperatures for 10 min. Finally, a layer of ~5 nm PFN was spin-coated using a methanol solution (mixed with 0.2% acetic acid, by volume)[37] onto the active layer and then an 80 nm Al layer was evaporated under high vacuum ($<2 \times 10^{-4}$ Pa). The effective areas of cells were 4 mm^2, defined by shallow masks.

For comparison, optimized devices with an effective area of 12 mm^2 were also fabricated and measured using an aperture of area 8.96 mm^2, which gave results similar to those for the 4 mm^2 devices described above. The J–V curves of photovoltaic devices were obtained using a Keithley 2400 source-measure unit in an argon-filled glove box. All I–V measurements with and without apertures gave consistent results, with relative errors within 5%. The photocurrent was measured under simulated 100 mW cm^{-2} AM 1.5G irradiation using an Oriel 96000 solar simulator, calibrated with a standard Si solar cell. The average PCE was obtained using 100 devices under the same conditions.

Received 12 January 2014; accepted 7 October 2014; published online 24 November 2014

References

1. He, Z. C. *et al.* Enhanced power-conversion efficiency in polymer solar cells using an inverted device structure. *Nature Photon.* **6,** 591–595 (2012).
2. Liao, S. H., Jhuo, H. J., Cheng, Y. S. & Chen, S. A. Fullerene derivative-doped zinc oxide nanofilm as the cathode of inverted polymer solar cells with low-bandgap polymer (PTB7-Th) for high performance. *Adv. Mater.* **25,** 4766–4771 (2013).
3. You, J. *et al.* A polymer tandem solar cell with 10.6% power conversion efficiency. *Nature Commun.* **4,** 1446 (2013).
4. Coughlin, J. E., Henson, Z. B., Welch, G. C. & Bazan, G. C. Design and synthesis of molecular donors for solution-processed high-efficiency organic solar cells. *Acc. Chem. Res.* **47,** 257–270 (2013).
5. Chen, Y., Wan, X. & Long, G. High performance photovoltaic applications using solution-processed small molecules. *Acc. Chem. Res.* **46,** 2645–2655 (2013).
6. Mishra, A. & Bäuerle, P. Small molecule organic semiconductors on the move: promises for future solar energy technology. *Angew. Chem. Int. Ed.* **51,** 2020–2067 (2012).
7. Zhou, J. *et al.* Solution-processed and high-performance organic solar cells using small molecules with a benzodithiophene unit. *J. Am. Chem. Soc.* **135,** 8484–8487 (2013).
8. Kyaw, A. K. K. *et al.* Improved light harvesting and improved efficiency by insertion of an optical spacer (ZnO) in solution-processed small-molecule solar cells. *Nano Lett.* **13,** 3796–3801 (2013).
9. Liu, Y. *et al.* Solution-processed small-molecule solar cells: breaking the 10% power conversion efficiency. *Sci. Rep.* **3,** 3356 (2013).
10. Heliatek. *Heliatek consolidates its technology leadership by establishing a new world record for organic solar technology with a cell efficiency of 12%*. Available at http://www.heliatek.com/wp-content/uploads/2013/01/130116_PR_Heliatek_achieves_record_cell_effiency_for_OPV.pdf. (January, 2013).
11. Steinmann, V. *et al.* Simple, highly efficient vacuum-processed bulk heterojunction solar cells based on merocyanine dyes. *Adv. Energy Mater.* **1,** 888–893 (2011).
12. Sun, Y. *et al.* Solution-processed small-molecule solar cells with 6.7% efficiency. *Nature Mater.* **11,** 44–48 (2012).
13. Walker, B., Kim, C. & Nguyen, T.-Q. Small molecule solution-processed bulk heterojunction solar cells. *Chem. Mater.* **23,** 470–482 (2010).
14. Jorgensen, M., Norrman, K. & Krebs, F. C. Stability/degradation of polymer solar cells. *Sol. Energy Mater. Sol. Cells* **92,** 686–714 (2008).
15. Blom, P. W., Mihailetchi, V. D., Koster, L. J. A. & Markov, D. E. Device physics of polymer: fullerene bulk heterojunction solar cells. *Adv. Mater.* **19,** 1551–1566 (2007).
16. Roncali, J. Molecular bulk heterojunctions: an emerging approach to organic solar cells. *Acc. Chem. Res.* **42,** 1719–1730 (2009).
17. Liang, Y. & Yu, L. A new class of semiconducting polymers for bulk heterojunction solar cells with exceptionally high performance. *Acc. Chem. Res.* **43,** 1227–1236 (2010).
18. Zhou, H., Yang, L. & You, W. Rational design of high performance conjugated polymers for organic solar cells. *Macromolecules* **45,** 607–632 (2012).
19. Li, Y. Molecular design of photovoltaic materials for polymer solar cells: toward suitable electronic energy levels and broad absorption. *Acc. Chem. Res.* **45,** 723–733 (2012).
20. Lin, Y., Li, Y. & Zhan, X. Small molecule semiconductors for high-efficiency organic photovoltaics. *Chem. Soc. Rev.* **41,** 4245–4272 (2012).
21. Brabec, C. J., Heeney, M., McCulloch, I. & Nelson, J. Influence of blend microstructure on bulk heterojunction organic photovoltaic performance. *Chem. Soc. Rev.* **40,** 1185–1199 (2011).
22. Liu, F. *et al.* Characterization of the morphology of solution-processed bulk heterojunction organic photovoltaics. *Prog. Polym. Sci.* **38,** 1990–2052 (2013).
23. Chen, L.-M., Xu, Z., Hong, Z. & Yang, Y. Interface investigation and engineering—achieving high performance polymer photovoltaic devices. *J. Mater. Chem.* **20,** 2575–2598 (2010).
24. Yip, H.-L. & Jen, A. K. Y. Recent advances in solution-processed interfacial materials for efficient and stable polymer solar cells. *Energy Environ. Sci.* **5,** 5994–6011 (2012).
25. He, Z., Wu, H. & Cao, Y. Recent advances in polymer solar cells: realization of high device performance by incorporating water/alcohol soluble conjugated polymers as electrode buffer layer. *Adv. Mater.* **26,** 1006–1024 (2014).
26. Kyaw, A. K. K. *et al.* Efficient solution processed small molecule solar cells with inverted structure. *Adv. Mater.* **25,** 2397–2402 (2013).
27. Li, X. *et al.* Dual plasmonic nanostructures for high performance inverted organic solar cells. *Adv. Mater.* **24,** 3046–3052 (2012).
28. Dou, L. *et al.* 25th anniversary article: A decade of organic/polymeric photovoltaic research. *Adv. Mater.* **25,** 6642–6671 (2013).
29. Li, Z. *et al.* Solution processable rhodanine-based small molecule organic photovoltaic cells with a power conversion efficiency of 6.1%. *Adv. Energy Mater.* **2,** 74–77 (2012).
30. Proctor, C. M., Kuik, M. & Nguyen, T.-Q. Charge carrier recombination in organic solar cells. *Prog. Polym. Sci.* **38,** 1941–1960 (2013).
31. Mao, J. *et al.* Stable dyes containing double acceptors without COOH as anchors for highly efficient dye-sensitized solar cells. *Angew. Chem. Int. Ed.* **124,** 10011–10014 (2012).
32. Kuo, M. Y., Chen, H. Y. & Chao, I. Cyanation: providing a three in one advantage for the design of n-type organic field-effect transistors. *Chem. Eur. J.* **13,** 4750–4758 (2007).
33. Brédas, J.-L., Beljonne, D., Coropceanu, V. & Cornil, J. Charge-transfer and energy-transfer processes in π-conjugated oligomers and polymers: a molecular picture. *Chem. Rev.* **104,** 4971–5004 (2004).
34. Park, S. H. *et al.* Bulk heterojunction solar cells with internal quantum efficiency approaching 100%. *Nature Photon.* **3,** 297–302 (2009).
35. Pettersson, L. A., Roman, L. S. & Inganas, O. Modeling photocurrent action spectra of photovoltaic devices based on organic thin films. *J. Appl. Phys.* **86,** 487–496 (1999).
36. Peumans, P., Yakimov, A. & Forrest, S. R. Small molecular weight organic thin-film photodetectors and solar cells. *J. Appl. Phys.* **93,** 3693–3723 (2003).
37. He, Z. C. *et al.* Simultaneous enhancement of open-circuit voltage, short-circuit current density, and fill factor in polymer solar cells. *Adv. Mater.* **23,** 4636–4643 (2011).
38. Long, G. *et al.* Impact of the electron-transport layer on the performance of solution-processed small-molecule organic solar cells. *ChemSusChem* **7,** 2358–2364 (2014).

39. Mandoc, M. M., Veurman, W., Koster, L. J. A., de Boer, B. & Blom, P. W. Origin of the reduced fill factor and photocurrent in MDMO-PPV:PCNEPV all polymer solar cells. *Adv. Funct. Mater.* **17,** 2167–2173 (2007).
40. Proctor, C. M., Kim, C., Neher, D. & Nguyen, T.-Q. Nongeminate recombination and charge transport limitations in diketopyrrolopyrrole-based solution-processed small molecule solar cells. *Adv. Funct. Mater.* **23,** 3584–3594 (2013).
41. Guerrero, A. *et al.* Solution-processed small molecule:fullerene bulk-heterojunction solar cells: impedance spectroscopy deduced bulk and interfacial limits to fill-factors. *Phys. Chem. Chem. Phys.* **15,** 16456–16462 (2013).
42. Lenes, M., Morana, M., Brabec, C. J. & Blom, P. W. Recombination limited photocurrents in low bandgap polymer/fullerene solar cells. *Adv. Funct. Mater.* **19,** 1106–1111 (2009).
43. Mozer, A. J. *et al.* Charge transport and recombination in bulk heterojunction solar cells studied by the photoinduced charge extraction in linearly increasing voltage technique. *Appl. Phys. Lett.* **86,** 112104 (2005).
44. Li, W. *et al.* Effect of the fibrillar microstructure on the efficiency of high molecular weight diketopyrrolopyrrole-based polymer solar cells. *Adv. Mater.* **26,** 1565–1570 (2014).
45. Guo, X. G. *et al.* Polymer solar cells with enhanced fill factors. *Nature Photon.* **7,** 825–833 (2013).
46. Chen, D., Liu, F., Wang, C., Nakahara, A. & Russell, T. P. Bulk heterojunction photovoltaic active layers via bilayer interdiffusion. *Nano Lett.* **11,** 2071–2078 (2011).

Acknowledgements

The authors acknowledge financial support from the Ministry of Science and Technology of China (MoST, 2014CB643502 and 2012CB933401), the National Natural Science Foundation of China (NSFC, 51373078) and the Program for Changjiang Scholars and Innovative Research Team in University (PCSIRT, IRT1257). The morphological characterization of the active layers was supported by the DOE-funded Energy Frontier Research Center on Polymer-Based Materials for Harvesting Solar Energy (DE-SC0001087). Portions of this research were carried out at the Advanced Light Source, Berkeley National Laboratory, which was supported by the DOE, Office of Science and Office of Basic Energy Sciences. The authors also acknowledge Beamline BL14B1 (Shanghai Synchrotron Radiation Facility) for providing beam time.

Author contributions

Y.C., Q.Z. and X.W. proposed and designed the project and Y.C. and X.W. directed the study. Q.Z. and M.L. fabricated and characterized the devices. B.K. synthesized most of the donor materials with help from W.N., Y.Z. and H.Z. F.L. and T.R. performed and analysed the GIXD and RSoXS film characterization. G.K. and M.Z. performed the DFT calculations and the optical simulations. X.C. and Z.L. performed the experiments on refractive index n and extinction coefficient k and photo-CELIV. Z.H., F.H. and Y.C. provided the PFN materials. All authors discussed the results and commented on the manuscript.

Additional information

Supplementary information is available in the online version of the paper. Reprints and permissions information is available online at www.nature.com/reprints. Correspondence and requests for materials should be addressed to Y.C.

Competing financial interests

A patent (application no. CN2014100099426) has been filed for the materials and devices.